

Softening of a flat phonon mode in the kagome ScV_6Sn_6

A. Korshunov,^{1,*} H. Hu,^{2,*} D. Subires,^{2,*} Y. Jiang,^{3,4,*} D. Călugăru,^{5,*} X. Feng,^{2,6,*} A. Rajapitamahuni,⁷ C. Yi,⁶ S. Roychowdhury,⁶ M. G. Vergniory,^{2,6} J. Strempler,⁸ C. Shekhar,⁶ E. Vescovo,⁷ D. Chernyshov,¹ A. H. Said,⁸ A. Bosak,¹ C. Felser,⁶ B. Andrei Bernevig,^{2,5,9,†} and S. Blanco-Canosa^{2,9,‡}

¹European Synchrotron Radiation Facility (ESRF), BP 220, F-38043 Grenoble

²Donostia International Physics Center (DIPC),

Paseo Manuel de Lardizábal. 20018, San Sebastián, Spain

³Beijing National Laboratory for Condensed Matter Physics, and Institute of Physics, Chinese Academy of Sciences, Beijing 100190, China

⁴University of Chinese Academy of Sciences, Beijing 100049, China

⁵Department of Physics, Princeton University, Princeton, NJ 08544, USA

⁶Max Planck Institute for Chemical Physics of Solids, 01187 Dresden, Germany

⁷National Synchrotron Light Source II, Brookhaven National Laboratory, Upton, New York 11973, USA

⁸Advanced Photon Source, Argonne National Laboratory, Lemont, IL 60439

⁹IKERBASQUE, Basque Foundation for Science, 48013 Bilbao, Spain

(Dated: April 2023)

The long range electronic modulations recently discovered in the geometrically frustrated kagome lattice have opened new avenues to explore the effect of correlations in materials with topological electron flat bands. Charge density waves (CDW), magnetism and superconducting phases are thought to be - depending on the electron number - the result of either the flat bands, the multiple Dirac crossings or the van Hove singularities close to the Fermi level. Nevertheless, the observation of the lattice response to the emergent new phases of matter, a soft phonon mode, has remained elusive and the microscopic origin of CDWs is still unknown. Here, we show, for the first time, a complete melting of the ScV_6Sn_6 (166) kagome lattice. The low energy longitudinal phonon with propagation vector $\frac{1}{3}\frac{1}{3}\frac{1}{2}$ collapses at 98 K, without the emergence of long-range charge order, which, remarkably, sets in with a propagation vector $\frac{1}{3}\frac{1}{3}\frac{1}{3}$. The CDW is driven (but locks at a different vector) by the softening of an overdamped phonon flat plane at $k_z=\pi$, characterized by an out-of-plane vibration of the trigonal Sn atoms. We observe broad phonon anomalies in momentum space, pointing to (1) the existence of approximately flat phonon bands which gain some dispersion due to electron renormalization, and (2) the effects of the momentum dependent electron-phonon interaction in the CDW formation. *Ab initio* and analytical calculations corroborate the experimental finding to indicate that the weak leading order phonon instability is located at the wave vector $\frac{1}{3}\frac{1}{3}\frac{1}{2}$ of a rather flat collapsed mode. In particular, we analytically compute the phonon frequency renormalization from high temperatures to the soft mode, and relate it to a peak in the orbital-resolved susceptibility of the trigonal Sn atoms, obtaining excellent match with both *ab initio* and experimental results, and explaining the origin of the approximately flat phonon dispersion. Our data report the first example of the collapse of a kagome bosonic mode (softening of a flat phonon plane) and promote the 166 compounds of the kagome family as primary candidates to explore correlated flat phonon-topological flat electron physics.

The search for quantum materials with novel forms of entangled fermion-fermion and fermion-boson interactions has led to the discovery of new emergent electronic phases of matter with charge order, epitomized in the family of high Tc superconductors [1, 2] and in the recently discovered hexagonal kagome metals [3–5]. The kagome lattice, hosting large electron densities of states at the Fermi level, has recently emerged as a rich platform to study the interplay between topology and correlated physics [6]. Topological flat bands derived from the destructive interference of the electronic wavefunction, van Hove singularities (vHs) at the Brillouin zone (BZ) boundary (M point) and Dirac crossings at

the BZ corner (K point) lurk at, beneath, and above the Fermi level [7, 8] depending on the electron number. *d*-electrons provide a path for interactions and the intertwining of different exotic orders. Among those, the interplay between multicomponent hexagonal charge density waves (CDWs) [9], magnetism [10, 11], nematic order [12] and superconductivity are extensively studied as candidates to explore strongly correlated topological physics. While the band structure is very complicated, and cannot be purely understood by the usual kagome flat band argument [13] which would give an incorrect counting of the number of flat bands in these *d*-orbital systems hybridized with *p* orbitals of close-by atoms [14], it is clear that both wavefunction topology and interactions are important for a wide range of these materials, such as FeGe and the 166 series MT_6Z_6 (M = metallic elements, such as Mg and rare-earth elements; T = transition metal, V, Cr, Mn, Fe, Co, Ni; Z = main group elements, Si, Ga,

* These authors contributed equally to this work.

† bernevig@princeton.edu

‡ sblanco@dipc.org

Ge, Sn) [15, 16].

Magnetism aside, strong attention is being paid to the AV_3Sb_5 ($A=K, Cs$ and Rb) system, hosting electronic ordering competing with superconductivity at lower temperature [17, 18]. Although further confirmation by Kerr and other probes is necessary, the CDW in AV_3Sb_5 (hereafter AVS) might break the mirror symmetry, defining an electronic chirality [19] that might additionally break the time reversal symmetry [20]. The AVS lattice dynamics across the multiple- q CDW is highly controversial, despite *ab initio* calculations which predict soft modes at M and L points of the BZ [21, 22]. The softening of a particular phonon branch is an elegant hallmark of the CDW transition, as first incarnated by Peierls in the perfectly nested Fermi surface of a 1-dimensional metal [23], and defines a soft lattice dynamics of a second order phase transition [24]. Nevertheless, the nesting scenario fails in higher dimensions; the electronic susceptibility does not fully diverge, the Fermi surface is not perfectly nested or the experimental q_{CDW} does not match the nesting wavevectors [25]. Initial arguments based on the scattering between saddle points in AVS were supported by the presence of nested components of the Fermi surface [26, 27], but signatures of the fermion-boson many body interplay (Kohn anomaly) are not manifested experimentally [28].

Alternatively, a periodic lattice distortion can also be stabilized in presence of a finite orbital and momentum dependent electron-phonon interaction (EPI) [29], provided that the electronic degrees of freedom enhance the electron-phonon matrix elements. The concept of momentum dependent EPI is strongly supported by the experimental data; a broad momentum spread of the phonon softening is observed by x-ray scattering [30–32], a large gap ratio ($\Delta/k_B T_{CDW}$) exceeding the BCS theory [33] or the presence of a pseudogap at $T > T_{CDW}$ [34, 35]. Following this argument, the dynamics of the CDW in AVS seems to follow an order-disorder transformation type (strong coupling limit) [36, 37] that leads to a first order phase transition and the absence of the lattice collapse at the critical temperature, T_{CDW} . The magnetic kagome FeGe also features a first-order like CDW transition [38] without phonon softening [39], but strongly intertwined with its magnetic order [40].

Very recently, a first order-like CDW with propagation vector $\frac{1}{3}\frac{1}{3}\frac{1}{3}$ has been observed in the ScV_6Sn_6 (hereafter SVS) kagome lattice (166 family) at $T_{CDW} = 95$ K [41], with similar filling of the V d-orbitals as AVS (importantly, away from the flat bands). However, unlike in AVS, the Sn p-bands in SVS contribute weakly (only through the trigonal and not hexagonal Sn) to the Fermi surface, thus the two vHs at M are derived from the d-orbitals of the V-sublayer. Initial ARPES data [42], supported by optical spectroscopy [43], revealed no energy gap at the Fermi level, in contrast to the 20 meV CDW gap observed by scanning tunneling spectroscopy (STM) [44]. Moreover, the comparison of different members of the 166 kagome family (some at different electron

number) with and without periodic modulations suggests an unconventional nature of the CDW, strongly coupled with its lattice dynamics [45]. This is particularly interesting, since the propagation vector of the charge modulations in SVS is not compatible with the scattering between high symmetry points of the BZ, marking a clear distinction with the primary order parameters of AVS and FeGe [46]. Furthermore, recent *ab initio* calculations show a rich landscape of lattice instabilities - yet physically not understood- where the Sc and Sn vibrations play a dominant role [47]. Nevertheless, despite intense efforts to microscopically understand the nature of the CDW phases in materials, a direct experimental and theoretical demonstration of the fermion-boson coupling in the lattice is still missing.

Here, we use a combination of high resolution inelastic x-ray (IXS) and diffuse scattering (DS), angle resolved photoemission spectroscopy (ARPES) and density functional theory (DFT) and analytical effective models to experimentally reveal and theoretically understand a softening of the $k_z = \pi$ plane of the ScV_6Sn_6 net following a mean field critical behavior. Remarkably, a phonon with propagation vector $\frac{1}{3}\frac{1}{3}\frac{1}{2}$ collapses at the same temperature, $T_{CDW} \sim 98$ K, as the long-range CDW order with propagation vector $\frac{1}{3}\frac{1}{3}\frac{1}{3}$ sets in. The softening of the low energy branch is broad in momentum space, unveiling a strong momentum dependence of the electron-phonon interaction (EPI) which only influences some phonons on certain parts of the Brillouin Zone (BZ). Hard x-ray diffraction and theoretical modelling revealed that the soft phonon driven condensation consists of a longitudinal mode characterized by an out-of-plane vibration of Sn1 located in the trigonal environment. This mode starts flat at high temperatures and acquires (small) dispersion due to the electron renormalization, as we show experimentally and theoretically through full *ab initio* calculations and simple effective field theory models.

We start with a brief overview of the structure and electronic band dispersion of SVS. Unlike AVS, where the Sb atoms lie in the V plane, the Sn (Sn1) atoms sit above and below the kagome net (cyan spheres in figure 1 (A) and (B)). Although this displacement does not corrugate the kagome plane, it actually introduces large modifications in their band structure, which becomes even more complicated due to four possible surface terminations: two V_3Sn with different bucklings, $ScSn_2$, and honeycomb Sn in the middle, among which only two are reported experimentally [48]. The Fermi surface (FS) topology measured at 7 K with 90 eV photons that probe the $k_z = 0.4$ plane of the bulk BZ is displayed in figure 1 (D). A large hexagonal FS centered at the $\bar{\Gamma}$ point is surrounded by large triangular features with d orbital character of V atoms. The measured band dispersions are shown along the high-symmetry direction in figure 1 (E,F), with the *ab initio* bands included in figure 1 (G) for comparison. In figure 1 (E,F), the dispersions along the $\bar{M} - \bar{K} - \bar{\Gamma}$ and $\bar{\Gamma} - \bar{M}$ segments are measured within two different samples, and a mismatch of about 100 meV can be observed

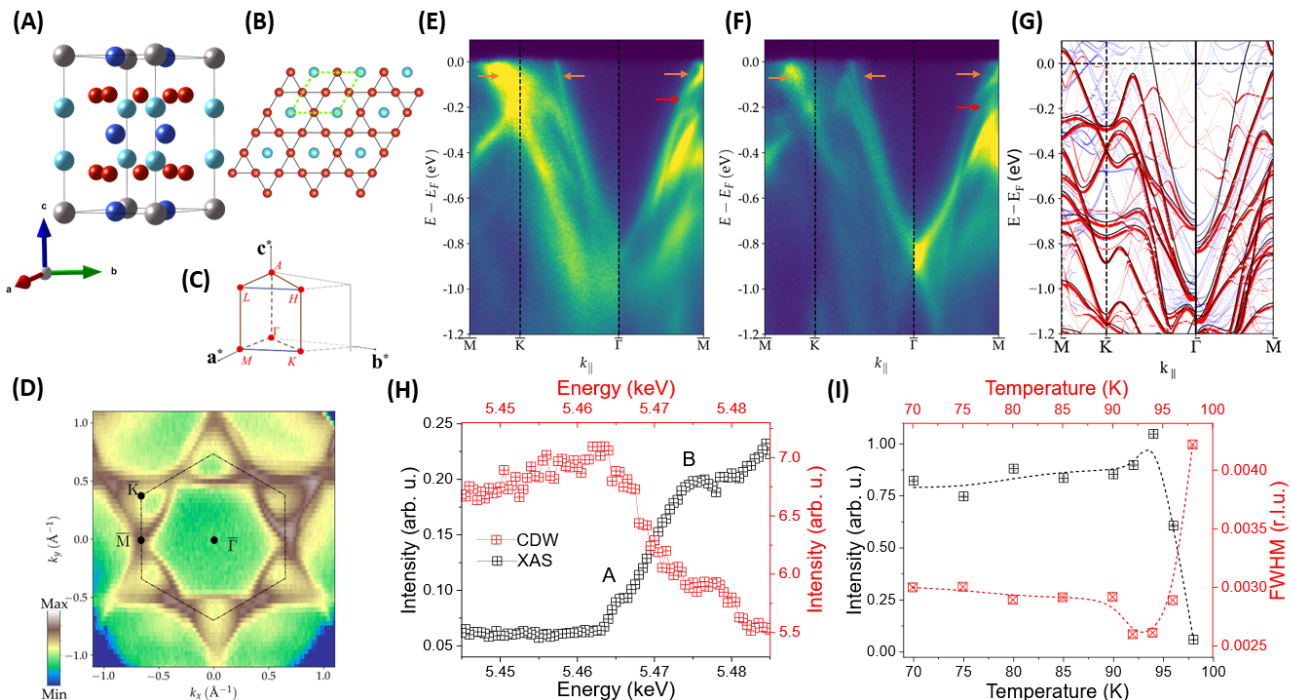


Figure 1. **Crystal and electronic band structure of ScV_6Sn_6 .** (A) Side view of the ScV_6Sn_6 structure. Red and grey balls stand for V atoms that define the kagome net and Sc, respectively. Cyan and blue denote the trigonal Sn1 and hexagonal Sn2 atoms. Note that the Sn1 atoms are lifted above and below the V kagome plane. (B) Top view of the kagome net, highlighting the V and Sn1 atoms. Green dashed lines denote the unit cell. (C) Brillouin zone of the space group $P6/mmm$ (191) and the main symmetry directions. (D) Fermi surface map of ScV_6Sn_6 at 7 K taken with horizontal polarized light and $E_i=90$ eV ($k_z=0.4 \text{ \AA}^{-1}$). (E) Band dispersions along the high symmetry direction $\bar{M}-\bar{K}-\bar{\Gamma}-\bar{M}$ acquired at 7 K with horizontal (H) and (F) vertical (V) polarized light (see Appendix). Orange and red arrows identify the surface states and the gap opening due to the avoided band crossing, respectively. (G) DFT calculations reproduce qualitatively the bulk and surface states of SVS, where black, red, and blue bands stand for the pristine bands, unfolded CDW bands, and surface bands, respectively. The bands along $\bar{M}-\bar{K}-\bar{\Gamma}$ are shifted upwards by 100 meV in order to match the ARPES bands. (H) Resonant hard x-ray scattering showing the energy profile of the $\frac{1}{3}\frac{1}{3}\frac{10}{3}$ CDW peak at the V K-edge. See the main text for the explanation of the A and B peaks. (I) Temperature dependence of the intensity and linewidth of the CDW peak at the V K-edge.

at the $\bar{\Gamma}$ point, around $E-E_F = -0.8$ eV. This mismatch arises probably due to the polar surface termination in one of the two samples. Consequently, we introduce an identical energy shift in the *ab initio* bands from figure 1 (G) and find that the computed band structure qualitatively reproduces the measured signal. Along the $\bar{\Gamma}-\bar{M}$ line, the *ab initio* bands that cross the Fermi level in the pristine phase (black lines) are absent in the experiment. Additionally, the signal suppression at ~ -0.2 eV from figure 1 (E,F) indicated by the red arrow matches the gap opening induced by the CDW phase. The apparent Dirac crossing at ~ -0.9 eV near the $\bar{\Gamma}$ point seen in figure 1 (F) stems from the symmetry-enforced suppression of the signal at the $\bar{\Gamma}$ point as a result of the interplay between the orbital character of the corresponding bands and the polarization of the incoming photons (see Appendix [49] for details). Finally, the surface states of SVS, shown by the orange arrow in figure 1 (E,F) and featuring prominent spectral weight in the vicinity of the Fermi level along the $\bar{M}-\bar{K}$ direction are consistent with

the *ab initio* calculations from figure 1 (G).

From our hard x-ray resonant diffraction data, figure 1 (H), we find CDW peaks at $h\pm\frac{1}{3}k\pm\frac{1}{3}l\pm\frac{1}{3}$, in agreement with the neutron diffraction data [41]. The absorption spectrum at the V K-edge (figure 1 (H)) exhibits a pre-edge feature (labelled as A), assigned to the dipole forbidden transition $1s\rightarrow 3d$ and a strong peak 15 eV above the pre-edge (B), assigned to the dipole-allowed transition $1s\rightarrow 4p$. Energy dependence of the CDW reflection shows a small resonant enhancement at the V pre-edge, which arises due to a combination of strong $3d$ - $4p$ mixing and overlap of the metal $3d$ orbitals with the $2p$ orbitals of Sn [50]. The CDW reflections start at ~ 98 K, with its maximum intensity at 92 K coinciding with T_{CDW} observed in resistivity and a maximum in-plane correlation length of 80 nm.

Next, we proceed our study with the analysis of the diffuse scattering (DS) maps, hunting for CDW precursors across the reciprocal space (RS). Figure 2 (A) shows the reconstructed maps spanning the $h-h/2$ plane at 300 K.

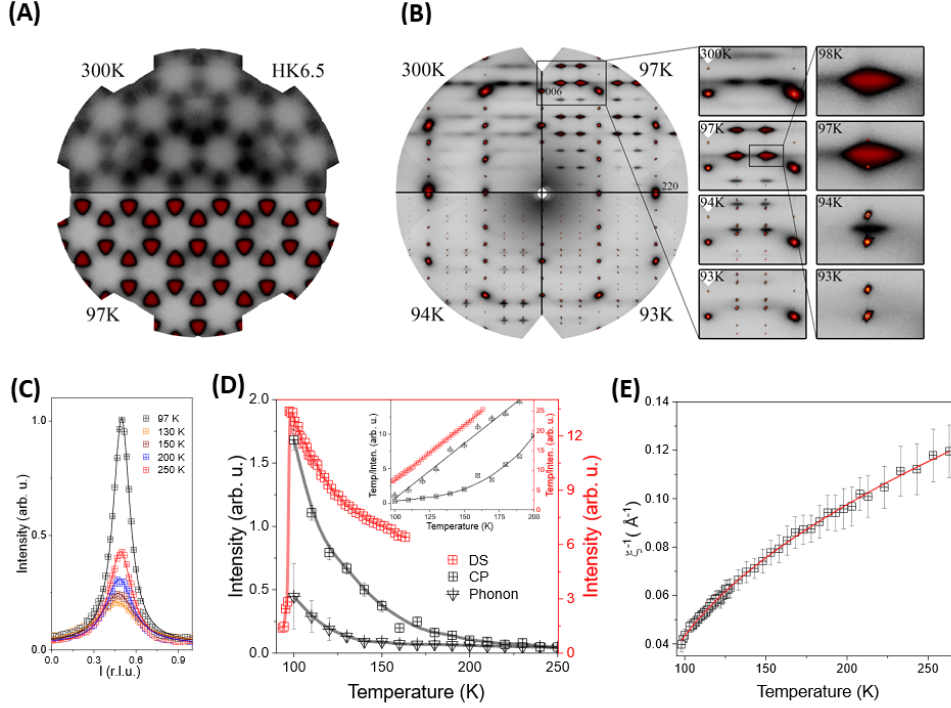


Figure 2. **Diffuse scattering maps of ScV_6Sn_6 .** (A) $h k 6.5$ plane at 300 K (top) and 100 K (bottom), showing the diffuse precursor of the 3D CDW at $l=\frac{1}{2}$ that grows in intensity upon cooling. (B) $h h l$ map, where no precursor is visible at $l=\frac{1}{3}$ at high temperature, but at $l=\frac{1}{2}$. The diffuse signal is replaced by the CDW Bragg satellites at low temperature, (right panels). (C) Temperature dependence of the diffuse scattering. Solid lines are fits to Lorentzian profiles. (D) Temperature dependence of the diffuse intensity, central peak (CP) and the low energy phonon at the $\frac{1}{3}\frac{1}{3}\frac{13}{2}$ position. Inset, temperature dependence of the generalized susceptibility. (E) Temperature dependence of the inverse of the diffuse correlation length. Solid line is the fitting to the mean field critical behavior, $\xi^{-1} = \xi_0^{-1}[(T - T_{\text{CDW}})/T_{\text{CDW}}]^\delta$ with $\delta = 0.49 \pm 0.02$.

Clear diffuse signals with triangular shape are visible at $h\pm\frac{1}{3} h\pm\frac{1}{3} l=\frac{1}{2}$ positions (H point) and grow in intensity upon cooling down to 100 K, below which it rapidly vanishes. On the other hand, no diffuse intensity is observed either with propagation vectors $\frac{1}{3}\frac{1}{3}\frac{1}{3}$, $\frac{1}{2}0\frac{1}{2}$ (L), $00\frac{1}{2}$ (A) [47], $\frac{1}{3}\frac{1}{3}0$ (K) and $\frac{1}{2}00$ (M) in the whole temperature range above T_{CDW} . Nevertheless, intense CDW reflections with propagation vector $\frac{1}{3}\frac{1}{3}\frac{1}{3}$ are observed below ~ 98 K, matching the x-ray data (Figure 1 (C)) and neutron scattering [41]. The reconstruction of the $h h l$ plane is displayed in the figure 2 (B) at several temperatures. Besides confirming the absence of DS at high temperature at $l=\frac{1}{3}$, the $l=\frac{1}{2}$ precursor increases its intensity with l , indicating that the DS is driven by the condensation of an out-of-plane polarized mode. Dissecting the anisotropic diffuse signal with cuts along the l and $h h$ directions around the $\mathbf{G}_{006}+(00\frac{1}{2})$ position (see Appendix for fitting details), reveals a strong dependence of its intensity and linewidth with temperature. The correlation length of the diffuse precursor at $l=\frac{1}{2}$ diverges upon cooling and extends to nearly 20 Å in the c -direction and less than one unit cell in the ab -plane at low temperature. The critical exponent of the inverse correlation length along

the c -direction, $\delta = 0.49 \pm 0.02$, follows the mean-field critical value and a mean-field critical behavior. In the temperature range between 100 and 95 K, both the DS at $l=\frac{1}{2}$ and CDW satellites at $l=\frac{1}{3}$ coexist. With further cooling, the diffuse precursor vanishes and only the CDW peaks remain.

In order to shed light on the microscopic origin of the DS at the $\frac{1}{3}\frac{1}{3}\frac{1}{2}$ reciprocal lattice vector, we have resolved the elastic and inelastic components of the scattered signal and study the low energy lattice dynamics by means of inelastic x-ray scattering (IXS). Figure 3 (A) compares the normalized IXS spectra with $\Delta E=3$ meV (see Appendix for representative scans with $\Delta E=1.5$ meV) as a function of temperature, focusing on the $\frac{1}{3}\frac{1}{3}\frac{13}{2}$ region of the RS, where the DS develops its maximum intensity. At 300 K, the IXS spectrum consists on 2 low energy Stokes and anti-Stokes longitudinal modes with frequency ~ 3 meV, which correspond to the out-of-plane polarized Sn1 atoms in trigonal coordination in the kagome lattice, according to our phonon calculations, see Appendix [49]. Their intensity grows upon cooling following the temperature behavior of the elastic central peak (CP, $E_{\text{loss}} \sim 0$ meV) of IXS, figure 2 (D), thus the diffuse intensity contains spectral weight from the CP and phonons. More-

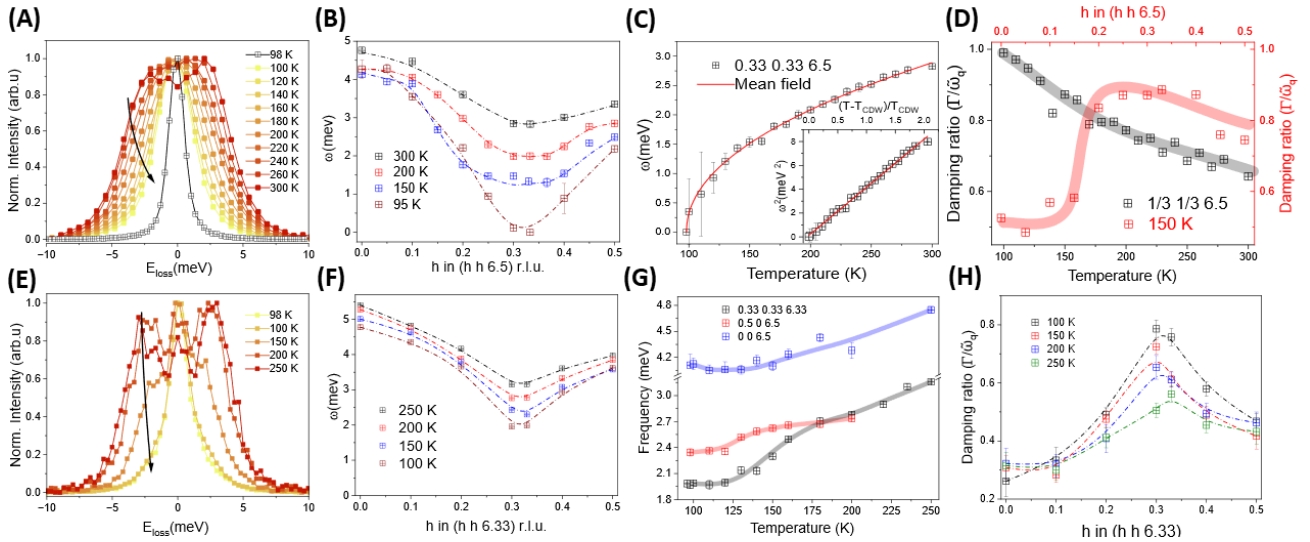


Figure 3. **Lattice dynamics of ScV_6Sn_6 .** (A) Normalized temperature dependence of the IXS spectra at the $\frac{1}{3} \frac{1}{3} \frac{13}{2}$ r.l.u. position with energy resolution $\Delta E=3$ meV. The normalized energy scan in black corresponds to the IXS scan with energy resolution of $\Delta E=1.5$ meV. See supplementary information for fitting details. (B) Momentum dependence of the $\frac{1}{3} \frac{1}{3} \frac{13}{2}$ phonon frequency at selected temperatures, highlighting the large momentum softening. (C) Temperature dependence of the soft mode and its fitting to a power law with $\alpha=0.47\pm 0.07$. Inset, linear behavior of the squared frequency *vs* reduced temperature. (D) Temperature (momentum at 150 K) dependence of the damping ratio, $\Gamma/\tilde{\omega}_q$, where Γ is the damping and $\tilde{\omega}_q$, the phonon frequency renormalized by the real part of the susceptibility. (E) IXS scans as a function of temperature at the $\frac{1}{3} \frac{1}{3} \frac{13}{2}$ r.l.u. position ($\Delta E=1.5$ meV). (F) Momentum dependence of the $\frac{1}{3} \frac{1}{3} \frac{19}{3}$ phonon frequency as a function of temperature. (G) Comparison of the temperature dependence of the $\frac{1}{3} \frac{1}{3} \frac{19}{3}$, $\frac{1}{2} 0 \frac{13}{2}$ and $0 0 \frac{13}{2}$ r.l.u. Acoustic branches are shown in the Appendix. (H) Momentum dependence of the phonon damping ratio at selected temperatures.

over, the generalized susceptibility, $\chi(\mathbf{q})$ (figure 2(D) inset), proportional to the \mathbf{q} Fourier component of the displacement-displacement correlation function [51], follows a linear Curie-Weiss behavior for the quasi-elastic component of the DS and the low energy phonon, unlike the CP that deviates from the linear behavior at high temperature.

On the other hand, the dispersion reveals an anomalous broad softening around $(h h)=(\frac{1}{3} \frac{1}{3})$ region of the momentum space, suggesting an incipient localization of the phonon fluctuations in real space (see Appendix for details of the fitting), not captured by the phonon calculations, which reveal a rather flat phonon band in the $k_z=\pi$ plane (and at other k_z 's). Similar \mathbf{q} -dependence of the lattice dynamics has been observed in NbSe_2 [30] and TiSe_2 [31] at $T>T_{\text{CDW}}$ and also in high T_c cuprates [52]. With further cooling, the momentum spread of the phonon softening acquires a U-shape, typical of systems which show an enhanced electron-phonon interaction (EPI), unlike the V-shape dispersion expected when the CDW is driven by the nesting of Fermi surface [24]. Nevertheless, although the low energy branch softens in a broad range of momenta, ~ 1 meV at the BZ center and ~ 2 meV at the BZ border, it only collapses at the critical wavevector $\mathbf{q}=\frac{1}{3} \frac{1}{3} \frac{1}{2}$ at $T_{\text{CDW}}=98$ K. The temperature dependence of the soft mode, plotted in the figure 3 (D), returns a critical exponent of 0.47 ± 0.07 , characteristic

of the mean field theory of phase transitions, and T_c of 98 K, as observed experimentally. This demonstrates that the soft lattice dynamics of SVS showcases the first example of the weak coupling limit theory of a second order phase transition within the kagome family. At the critical temperature the IXS spectrum consists of a resolution limited elastic line central peak at zero energy loss and the phonon is no longer resolvable, see Appendix. On the other hand, the damping ratio of the soft mode increases upon cooling and becomes critically overdamped at the critical temperature (figure 3 (D)), where phonons do not oscillate but only decay in time. Besides, the longitudinal low energy branch develops an anomalous broadening at high momentum transfers ($0.15<h h<0.5$ r.l.u.) with a damping ratio close to its critical value.

Having identified and characterized the dynamics of the soft mode, we now turn our attention to the lattice dynamics at the $\frac{1}{3} \frac{1}{3} \frac{1}{3}$ reciprocal lattice vector, where the electronic modulations develop at low temperature. In figure 3 (E), we present the temperature dependence of the normalized raw spectra at the $\frac{1}{3} \frac{1}{3} \frac{19}{3}$ lattice vector. The mode with an energy of 3 meV ($\Delta E=1.5$ meV) is better resolvable and gradually softens throughout the entire region of momenta (~ 0.6 meV at the center and border of the BZ and ~ 1.2 meV at the q_{CDW}) (figure 3 (F)), but, without collapsing to zero frequency at the critical temperature. Although the dispersion of the mode

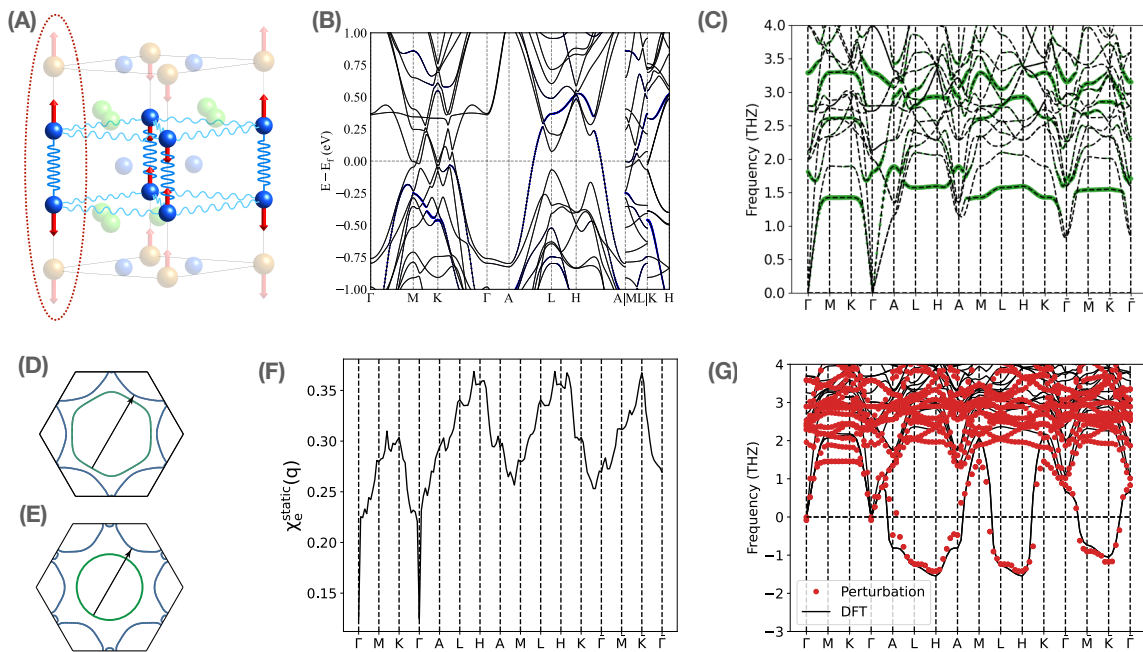


Figure 4. **Phonon spectrum, Band structure, Fermi surface nesting and charge susceptibility of ScV_6Sn_6 .** (A) Vibration mode of the imaginary phonon mode at $\frac{1}{3}\frac{1}{3}\frac{1}{2}$. The phonon spectrum can be described by a series of weakly-coupled 1D chains where the dashed red line marks one of the 1D chains. The z -direction vibration mode of the Sn atom is only weakly coupled to the z -direction vibration modes of the other Sn atom within the same plane since the displacement between two atoms is perpendicular to the direction of vibration. (B) Band structure of the pristine phase where the blue dots mark the weight of Sn p_z orbitals. (C) High-temperature (non-interacting) phonon spectrum derived from DFT at $T = 1.2\text{eV}$. The green dots mark the weights of the z -direction vibration of trigonal Sn atoms, where we observe an extremely flat low-energy phonon band that is mostly formed by the z -direction vibration of trigonal Sn atoms. (D) Fermi surfaces at $k_z = -0.32$ (green) and $k_z = 0.18$ (blue) where we observe a weak nesting near $H = \frac{1}{3}\frac{1}{3}\frac{1}{2}$ (the exact nesting vector is $(0.4, 0.4, 0.5)$). (E) Fermi surfaces at $k_z = 0.20$ (green) and $k_z = 0.53$ (blue) where we observe a weak nesting with nesting vector $\bar{K} = \frac{1}{3}\frac{1}{3}\frac{1}{3}$. (F) Static charge susceptibility of the mirror-even electron operator $c_{\mathbf{R},e,\sigma}$. (G) Phonon spectrum derived from DFT at zero temperature and from perturbation theory by combining the non-interacting phonon spectrum with electron correction. Both methods predict a relatively flat imaginary mode at $k_z = \frac{1}{2}$ with leading-order instability at the wavevector $(\frac{1}{3}\frac{1}{3}\frac{1}{2})$ where we observe phonon collapsing experimentally.

follows a more classic V-shape even at room temperature, its frequency remains finite at ~ 1.5 meV below 125 K and down to the critical temperature. Below T_{CDW} , the large enhancement of the elastic line, which drives the phase transition, completely masks the phonon and precludes its analysis. However, similar to the $l=\frac{1}{2}$ branch, the phonon again approaches the critical damping value, demonstrating its coupling to electronic degrees of freedom. Indeed, the extraordinary coupling of electrons to the lattice is not only limited to the softening of the $l=\frac{1}{2}$ and $\frac{1}{3}$ branches, but also to the lattice vibrations at the A and L points of the BZ. The temperature dependence of the $0\ 0\ 6.5$ and $0.5\ 0\ 6.5$ modes, also involving the out of plane vibration of the trigonal Sn atoms, are displayed in the figure 3 (G), showing a moderate softening from room temperature down to 125 K, thus demonstrating experimentally the richness of lattice instabilities explained by our calculations Appendix.

We now provide a theoretical understanding of the soft phonon modes. More and full details are found in Ap-

pendix [49] and Ref. [53]. To begin with, in figure 4 (C), we show the high-temperature phonon spectrum derived from our DFT calculation, which can also be understood as a non-interacting phonon spectrum where the renormalization from electron-phonon coupling almost vanishes. We observe the low-energy phonon branch, which will collapse at low temperatures, is extremely flat in most parts of the Brillouin zone and is formed mostly by the z -direction vibration of trigonal Sn atoms (figure 4 (C)). The flatness feature indicates the non-interacting phonon model can be described by a series of weakly coupled one-dimensional chains (as illustrated in figure 4 (A)) formed by the trigonal Sn atoms which are the heaviest atoms of the system and contribute most to the low-energy phonon mode. As we will show later, the picture of weakly coupled 1D chains still holds (with some acquired finite in-plane dispersion) even at low temperature where significant renormalization from electrons appears.

Based on a recently introduced physical Gaussian ap-

proximation [54] and perturbation theory, we are able to analytically derive the electron correction to the non-interaction phonon spectrum [49, 53]. The resulting phonon spectrum is shown in the figure. 4 (G) with a comparison to the DFT-calculated phonon spectrum at zero temperature. We observe a good match, where both predict an imaginary phonon spectrum that is more dispersive (but still relatively flat) than the non-interacting phonon spectrum with a leading order instability at experimentally observed phonon collapsing wave vector $\mathbf{H} = \frac{1}{3}\frac{1}{3}\frac{1}{2}$.

Remarkably, we are able to analytically prove that the major correction to the non-interacting phonon spectrum originates from the coupling between the mirror-even phonon field $u_{ez}(\mathbf{R})$ and the density operator of mirror-even electron field $c_{\mathbf{R},e,\sigma}$, where $u_{ez}(\mathbf{R})$ and $c_{\mathbf{R},e,\sigma}$ are both even under mirror- z transformation and are defined as

$$\begin{aligned} u_{ez}(\mathbf{R}) &= (u_{Sn_1^T,z}(\mathbf{R}) - u_{Sn_2^T,z}(\mathbf{R}))/\sqrt{2} \\ c_{\mathbf{R},e,\sigma} &= (c_{\mathbf{R},(Sn_1^T,p_z),\sigma} - c_{\mathbf{R},(Sn_2^T,p_z),\sigma})/\sqrt{2} \end{aligned} \quad (1)$$

where $u_{Sn_{1,2}^T,z}(\mathbf{R})$ denotes the phonon fields that characterize the z direction movement of two trigonal Sn atoms respectively, and $c_{\mathbf{R},(Sn_{1,2}^T,p_z),\sigma}$ denote the electron operator with p_z orbital and spin σ at two trigonal Sn atoms respectively (see the figure. 4 (B) for the band structure and weight of p_z orbital of trigonal Sn atom). The $u_{ez}(\mathbf{R})$ field at unit-cell \mathbf{R} represents the superposition of z -direction vibrations of two trigonal Sn atoms within the same unit cell. The minus sign in the definition of $u_{ez}(\mathbf{R})$ in Eq. 1 marks the opposite moving direction of two trigonal Sn atoms. Via the electron-phonon coupling, the charge fluctuations of mirror-even electron orbitals $c_{\mathbf{R},e,\sigma}$, which is characterized by the static charge susceptibility $\chi_e^{static}(\mathbf{q})$, will introduce a strong normalization to the $u_{ez}(\mathbf{R})$ phonon fields.

In figure. 4 (F), we show the behavior of static charge susceptibility χ_e^{static} , where we find two peaks, with one near $\mathbf{H} = \frac{1}{3}\frac{1}{3}\frac{1}{2}$ point and the other one near $\bar{\mathbf{K}} = \frac{1}{3}\frac{1}{3}\frac{1}{3}$ point. The enhancement of susceptibility near \mathbf{H} and at $\bar{\mathbf{K}}$ are attributed to the weak Fermi surface nesting as illustrated[55] in figure 4 (D) (E). Even though we identify the peak structures in the $\chi_e^{static}(\mathbf{q})$, the peaks are weak and the overall susceptibility does not show a strong momentum dependency. Consequently, after transforming to the real space, the charge susceptibility can be approximately described by $\chi^e(\mathbf{R}) \approx \chi^{on-site}\delta_{\mathbf{R},\mathbf{0}} + \sum_{i=1,\dots,6} \chi^{xy}\delta_{\mathbf{R},\mathbf{R}_i^{xy}} + \sum_{i=1,2} \chi^z\delta_{\mathbf{R},\mathbf{R}_i^z}$, which consists of a strong on-site term $\chi^{on-site}$, a relatively weak nearest-neighbor in-plane term (χ^{xy}) and also a weak nearest-neighbor out-of-plane term (χ^z). \mathbf{R}_i^{xy} and \mathbf{R}_i^z characterize the in-plane and out-of-plane nearest-neighbor sites respectively. The on-site fluctuations $\chi^{on-site}$ lower the energy of u_{ez} at all the momentum points, which is the main reason for the phonon collapsing. However, due to the inter-unit-cell coupling (along- z direction) between trigonal Sn phonon fields which comes from both the

non-interacting phonon model and the electron correction induced by χ^z , the phonon spectrum realizes a minimum at $k_z = \frac{1}{2}$ plane and has a relatively flat imaginary phonon mode in the whole $k_z = \frac{1}{2}$ plane, which are mostly formed by the u_{ez} phonon field. The relatively weak in-plane correlation χ^{xy} will only introduce a weak coupling between the 1D phonon chains and select the \mathbf{H} points to be the leading-order instability. Finally, we mention that, at $\bar{\mathbf{K}} = \frac{1}{3}\frac{1}{3}\frac{1}{3}$, χ^e also has a peak. However, the low-branch phonon bands at $k_z = \frac{1}{3}$ have less weight of $u_{ez}(\mathbf{R})$ compared to the low-branch phonon bands at $k_z = \frac{1}{2}$ due to the z -direction inter-unit cell coupling between the tridiagonal Sn phonon fields. Consequently, the low-branch phonon mode at $k_z = \frac{1}{3}$ experiences less renormalization from electron-phonon coupling and the dominant instability still locates at $k_z = \frac{1}{2}$ plane.

In summary, we conclude the low-energy phonon spectrum can be described by a series of weakly-coupled 1D chains (at both high and – less so – at low temperatures), where the electron-phonon coupling and the charge fluctuation of the mirror-even orbital $c_{\mathbf{R},e,\sigma}$ drive the flat imaginary phonon modes at $k_z = \frac{1}{2}$ plane with the leading-order instability at the experimentally-observed collapsing wavevector $\mathbf{H} = \frac{1}{3}\frac{1}{3}\frac{1}{2}$, in agreement with the *ab initio* results and analytical effective models.

Methods High-quality single crystals of ScV_6Sn_6 were grown by flux method [41] using high purity starting elements. Sc, V and Sn were mixed in the molar ratio Sc:V:Sn of 1:6:60. We loaded all materials into an alumina crucible that was sealed inside a quartz tube under vacuum (10^{-5} Torr). The tube was heated to 1100 °C over 10 h, soaked for 24 h, and then slowly cooled to 700 °C over 400 h. After centrifuging at 700 °C to remove excess Sn, the crystals were collected. Scanning electron microscopy with an energy-dispersive EDAX analyzer was used to determine the composition of the ScV_6Sn_6 crystal.

Diffuse scattering measurements (energy $E_i=17.8$ keV) were performed at the ID28 beamline at the European Synchrotron Research Facility (ESRF) with a Dectris PILATUS3 1M X area detector. The CrysAlis software package was used for the orientation matrix refinement and reciprocal space reconstructions. Low energy phonons were measured by inelastic x-ray scattering (IXS) at the ID28 IXS station at ESRF ($E_i=17.8$ keV, $\Delta E=3$ meV) and at the HERIX beamline at the Argonne Photon Source (APS) ($E_i=23.72$ keV, $\Delta E=1.5$ meV). The components ($h k l$) of the scattering vector are expressed in reciprocal lattice units (r.l.u.), ($h k l$) = $h\mathbf{a}^* + k\mathbf{b}^* + l\mathbf{c}^*$, where \mathbf{a}^* , \mathbf{b}^* , and \mathbf{c}^* are the reciprocal lattice vectors.

ARPES experiments were performed at the ESM-ARPES beamline at the NSLS II synchrotron equipped with a Scienta DA30 electron energy analyzer. The samples were cleaved inside an ultra-high vacuum chamber with a base pressure better than $\sim 4 \times 10^{-10}$ torr and $T=7$ K. The photon energy was scanned from 70 eV to 120 eV, from which we determine Γ and A points of the BZ. The

energy and momentum resolutions were better than 5 meV and 0.01 \AA^{-1} .

Resonant hard x-ray resonant scattering experiments were performed at the beamline 4ID-D of the Advanced Photon Source at Argonne National Laboratory. The ScV_6Sn_6 crystal was glued in a Cu sample holder and cooled in a close cycle cryostat.

The *ab initio* band structures are computed using the Vienna *ab initio* Simulation Package (VASP)[56–60], where the generalized gradient approximation (GGA) of the Perdew–Burke–Ernzerhof (PBE)-type[61] exchange-

correlation potential is used. A $8 \times 8 \times 6$ Γ -centered Monkhorst–Pack grid is adopted with a plane-wave energy cutoff of 400 eV. Wannier90[62–65] is used to construct maximally localized Wannier functions (MLWFs) for both the pristine and the CDW phases by considering the Sc d , V d , and Sn p orbitals. *WannierTools*[66] is used to post-process the tight-binding model obtained from Wannier90.

Data availability Source data are provided with this paper. The DS and IXS data generated in this study will be deposited in the Figshare database.

-
- [1] B. Keimer, S. A. Kivelson, M. R. Norman, S. Uchida, and J. Zaanen, From quantum matter to high-temperature superconductivity in copper oxides, *Nature* **518**, 179 (2015).
- [2] R. M. Fernandes, A. I. Coldea, H. Ding, I. R. Fisher, P. J. Hirschfeld, and G. Kotliar, Iron pnictides and chalcogenides: a new paradigm for superconductivity, *Nature* **601**, 35 (2022).
- [3] B. R. Ortiz, L. C. Gomes, J. R. Morey, M. Winiarski, M. Bordelon, J. S. Mangum, I. W. Oswald, J. A. Rodriguez-Rivera, J. R. Neilson, S. D. Wilson, *et al.*, New kagome prototype materials: discovery of kv 3 sb 5, rbv 3 sb 5, and csv 3 sb 5, *Physical Review Materials* **3**, 094407 (2019).
- [4] X. Teng, L. Chen, F. Ye, E. Rosenberg, Z. Liu, J.-X. Yin, Y.-X. Jiang, J. S. Oh, M. Z. Hasan, K. J. Neubauer, *et al.*, Discovery of charge density wave in a kagome lattice antiferromagnet, *Nature* **609**, 490 (2022).
- [5] H. W. S. Arachchige, W. R. Meier, M. Marshall, T. Matsumoto, R. Xue, M. A. McGuire, R. P. Hermann, H. Cao, and D. Mandrus, Charge density wave in kagome lattice intermetallic ScV_6Sn_6 , *Physical Review Letters* **129**, 216402 (2022).
- [6] I. I. Mazin, H. O. Jeschke, F. Lechermann, H. Lee, M. Fink, R. Thomale, and R. Valentí, Theoretical prediction of a strongly correlated dirac metal, *Nature Communications* **5**, 4261 (2014).
- [7] M. L. Kiesel, C. Platt, and R. Thomale, Unconventional fermi surface instabilities in the kagome hubbard model, *Phys. Rev. Lett.* **110**, 126405 (2013).
- [8] W.-S. Wang, Z.-Z. Li, Y.-Y. Xiang, and Q.-H. Wang, Competing electronic orders on kagome lattices at van hove filling, *Phys. Rev. B* **87**, 115135 (2013).
- [9] H. Zhao, H. Li, B. R. Ortiz, S. M. L. Teicher, T. Park, M. Ye, Z. Wang, L. Balents, S. D. Wilson, and I. Zeljkovic, Cascade of correlated electron states in the kagome superconductor csv3sb5, *Nature* **599**, 216 (2021).
- [10] J.-X. Yin, W. Ma, T. A. Cochran, X. Xu, S. S. Zhang, H.-J. Tien, N. Shumiya, G. Cheng, K. Jiang, B. Lian, Z. Song, G. Chang, I. Belopolski, D. Multer, M. Litskevich, Z.-J. Cheng, X. P. Yang, B. Swidler, H. Zhou, H. Lin, T. Neupert, X. Wang, N. Yao, T.-R. Chang, S. Jia, and M. Zahid Hasan, Quantum-limit chern topological magnetism in tbmn_6sn_6 , *Nature* **583**, 533 (2020).
- [11] H. Li, H. Zhao, B. R. Ortiz, T. Park, M. Ye, L. Balents, Z. Wang, S. D. Wilson, and I. Zeljkovic, Rotation symmetry breaking in the normal state of a kagome superconductor kv3sb5, *Nature Physics* **18**, 265 (2022).
- [12] Y. Xu, Z. Ni, Y. Liu, B. R. Ortiz, Q. Deng, S. D. Wilson, B. Yan, L. Balents, and L. Wu, Three-state nematicity and magneto-optical kerr effect in the charge density waves in kagome superconductors, *Nature Physics* **18**, 1470 (2022).
- [13] A. Mielke, Ferromagnetism in the hubbard model on line graphs and further considerations, *Journal of Physics A: Mathematical and General* **24**, 3311 (1991).
- [14] Y. Jiang, H. Hu, D. Călugăru, X. Yuanfeng, and B. A. Bernevig, To be published.
- [15] G. Venturini, Filling the cosn host-cell: the hffe6ge6-type and the related structures, *Zeitschrift für Kristallographie-Crystalline Materials* **221**, 511 (2006).
- [16] D. C. Fredrickson, S. Lidin, G. Venturini, B. Malaman, and J. Christensen, Origins of superstructure ordering and incommensurability in stuffed cosn-type phases, *Journal of the American Chemical Society* **130**, 8195 (2008).
- [17] B. R. Ortiz, S. M. L. Teicher, Y. Hu, J. L. Zuo, P. M. Sarte, E. C. Schueller, A. M. M. Abeykoon, M. J. Krogstad, S. Rosenkranz, R. Osborn, R. Seshadri, L. Balents, J. He, and S. D. Wilson, Cvs3sb5: A F_2 topological kagome metal with a superconducting ground state, *Phys. Rev. Lett.* **125**, 247002 (2020).
- [18] B. R. Ortiz, P. M. Sarte, E. M. Kenney, M. J. Graf, S. M. L. Teicher, R. Seshadri, and S. D. Wilson, Superconductivity in the F_2 kagome metal kv3sb5, *Phys. Rev. Materials* **5**, 034801 (2021).
- [19] C. Guo, C. Putzke, S. Konyzheva, X. Huang, M. Gutierrez-Amigo, I. Errea, D. Chen, M. G. Vergniory, C. Felser, M. H. Fischer, T. Neupert, and P. J. W. Moll, Switchable chiral transport in charge-ordered kagome metal csv3sb5, *Nature* **611**, 461 (2022).
- [20] C. Mielke, D. Das, J.-X. Yin, H. Liu, R. Gupta, Y.-X. Jiang, M. Medarde, X. Wu, H. C. Lei, J. Chang, P. Dai, Q. Si, H. Miao, R. Thomale, T. Neupert, Y. Shi, R. Khasanov, M. Z. Hasan, H. Luetkens, and Z. Guguchia, Time-reversal symmetry-breaking charge order in a kagome superconductor, *Nature* **602**, 245 (2022).
- [21] H. Tan, Y. Liu, Z. Wang, and B. Yan, Charge density waves and electronic properties of superconducting kagome metals, *Phys. Rev. Lett.* **127**, 046401 (2021).
- [22] A. Subedi, Hexagonal-to-base-centered-orthorhombic $4q$ charge density wave order in kagome metals kv3sb5, rbv3sb5, and csv3sb5, *Phys. Rev. Mater.* **6**, 015001 (2022).

- (2022).
- [23] R. Peierls, *Quantum Theory of Solids* (Oxford University Press, 1955).
- [24] M. Hoesch, A. Bosak, D. Chernyshov, H. Berger, and M. Krisch, Giant kohn anomaly and the phase transition in charge density wave zrte_3 , *Phys. Rev. Lett.* **102**, 086402 (2009).
- [25] M. D. Johannes and I. I. Mazin, Fermi surface nesting and the origin of charge density waves in metals, *Phys. Rev. B* **77**, 165135 (2008).
- [26] M. Kang, S. Fang, J.-K. Kim, B. R. Ortiz, S. H. Ryu, J. Kim, J. Yoo, G. Sangiovanni, D. Di Sante, B.-G. Park, C. Jozwiak, A. Bostwick, E. Rotenberg, E. Kaxiras, S. D. Wilson, J.-H. Park, and R. Comin, Twofold van hove singularity and origin of charge order in topological kagome superconductor csv_3sb_5 , *Nature Physics* **18**, 301 (2022).
- [27] Y.-X. Jiang, J.-X. Yin, M. M. Denner, N. Shumiya, B. R. Ortiz, G. Xu, Z. Guguchia, J. He, M. S. Hossain, X. Liu, J. Ruff, L. Kautzsch, S. S. Zhang, G. Chang, I. Belopolski, Q. Zhang, T. A. Cochran, D. Multer, M. Litskevich, Z.-J. Cheng, X. P. Yang, Z. Wang, R. Thomale, T. Neupert, S. D. Wilson, and M. Z. Hasan, Unconventional chiral charge order in kagome superconductor kv_3sb_5 , *Nature Materials* **20**, 1353 (2021).
- [28] H. Li, T. T. Zhang, T. Yilmaz, Y. Y. Pai, C. E. Marvinney, A. Said, Q. W. Yin, C. S. Gong, Z. J. Tu, E. Vescovo, C. S. Nelson, R. G. Moore, S. Murakami, H. C. Lei, H. N. Lee, B. J. Lawrie, and H. Miao, Observation of unconventional charge density wave without acoustic phonon anomaly in kagome superconductors AV_3sb_5 ($a = \text{Rb, cs}$), *Phys. Rev. X* **11**, 031050 (2021).
- [29] F. Flicker and J. van Wezel, Charge order from orbital-dependent coupling evidenced by nbse_2 , *Nature Communications* **6**, 7034 (2015).
- [30] F. Weber, S. Rosenkranz, J.-P. Castellán, R. Osborn, R. Hott, R. Heid, K.-P. Bohnen, T. Egami, A. H. Said, and D. Reznik, Extended phonon collapse and the origin of the charge-density wave in $2h\text{-nbse}_2$, *Phys. Rev. Lett.* **107**, 107403 (2011).
- [31] F. Weber, S. Rosenkranz, J.-P. Castellán, R. Osborn, G. Karapetrov, R. Hott, R. Heid, K.-P. Bohnen, and A. Alatas, Electron-phonon coupling and the soft phonon mode in tise_2 , *Phys. Rev. Lett.* **107**, 266401 (2011).
- [32] J. Diego, A. H. Said, S. K. Mahatha, R. Bianco, L. Monacelli, M. Calandra, F. Mauri, K. Rossnagel, I. Errea, and S. Blanco-Canosa, van der waals driven anharmonic melting of the 3d charge density wave in vse_2 , *Nature Communications* **12**, 598 (2021).
- [33] J. Feng, D. Biswas, A. Rajan, M. D. Watson, F. Mazzola, O. J. Clark, K. Underwood, I. Marković, M. McLaren, A. Hunter, D. M. Burn, L. B. Duffy, S. Barua, G. Balakrishnan, F. Bertran, P. Le Fèvre, T. K. Kim, G. van der Laan, T. Hesjedal, P. Wahl, and P. D. C. King, Electronic structure and enhanced charge-density wave order of monolayer vse_2 , *Nano Letters* **18**, 4493 (2018).
- [34] S. V. Borisenko, A. A. Kordyuk, A. N. Yaresko, V. B. Zabolotnyy, D. S. Inosov, R. Schuster, B. Büchner, R. Weber, R. Follath, L. Patthey, and H. Berger, Pseudogap and charge density waves in two dimensions, *Phys. Rev. Lett.* **100**, 196402 (2008).
- [35] B. Loret, N. Auvray, Y. Gallais, M. Cazayous, A. Forget, D. Colson, M.-H. Julien, I. Paul, M. Civelli, and A. Sacuto, Intimate link between charge density wave, pseudogap and superconducting energy scales in cuprates, *Nature Physics* **15**, 771 (2019).
- [36] D. Subires, A. Korshunov, A. H. Said, L. Sánchez, B. R. Ortiz, S. D. Wilson, A. Bosak, and S. Blanco-Canosa, Order-disorder charge density wave instability in the kagome metal $(\text{cs,rb})\text{v}_3\text{sb}_5$, *Nature Communications* **14**, 1015 (2023).
- [37] N. Ratcliff, L. Hallett, B. R. Ortiz, S. D. Wilson, and J. W. Harter, Coherent phonon spectroscopy and interlayer modulation of charge density wave order in the kagome metal csv_3sb_5 , *Phys. Rev. Mater.* **5**, L111801 (2021).
- [38] X. Teng, L. Chen, F. Ye, E. Rosenberg, Z. Liu, J.-X. Yin, Y.-X. Jiang, J. S. Oh, M. Z. Hasan, K. J. Neubauer, B. Gao, Y. Xie, M. Hashimoto, D. Lu, C. Jozwiak, A. Bostwick, E. Rotenberg, R. J. Birgeneau, J.-H. Chu, M. Yi, and P. Dai, Discovery of charge density wave in a kagome lattice antiferromagnet, *Nature* **609**, 490 (2022).
- [39] H. Miao, T. T. Zhang, H. X. Li, G. Fabbri, A. H. Said, R. Tartaglia, T. Yilmaz, E. Vescovo, J.-X. Yin, S. Murakami, L. X. Feng, K. Jiang, X. L. Wu, A. F. Wang, S. Okamoto, Y. L. Wang, and H. N. Lee, Spin-phonon coupling driven charge density wave in a kagome magnet, [arXiv:2210.06359](https://arxiv.org/abs/2210.06359).
- [40] X. Teng, J. S. Oh, H. Tan, L. Chen, J. Huang, B. Gao, J.-X. Yin, J.-H. Chu, M. Hashimoto, D. Lu, C. Jozwiak, A. Bostwick, E. Rotenberg, G. E. Granroth, B. Yan, R. J. Birgeneau, P. Dai, and M. Yi, Magnetism and charge density wave order in kagome fege , *Nature Physics* [10.1038/s41567-023-01985-w](https://doi.org/10.1038/s41567-023-01985-w) (2023).
- [41] H. W. S. Arachchige, W. R. Meier, M. Marshall, T. Matsuoka, R. Xue, M. A. McGuire, R. P. Hermann, H. Cao, and D. Mandrus, Charge density wave in kagome lattice intermetallic scv_6sn_6 , *Phys. Rev. Lett.* **129**, 216402 (2022).
- [42] S.-H. Kang, H. Li, W. R. Meier, J. W. Villanova, S. Hus, H. Jeon, H. W. S. Arachchige, Q. Lu, Z. Gai, J. Denlinger, R. Moore, M. Yoon, and D. Mandrus, Emergence of a new band and the lifshitz transition in kagome metal scv_6sn_6 with charge density wave, [arXiv:2302.14041](https://arxiv.org/abs/2302.14041).
- [43] T. Hu, H. Pi, S. Xu, L. Yue, Q. Wu, Q. Liu, S. Zhang, R. Li, X. Zhou, J. Yuan, D. Wu, T. Dong, H. Weng, and N. Wang, Optical spectroscopy and band structure calculations of structural phase transition in the vanadium-based kagome metal scv_6sn_6 , [arXiv:2211.03412](https://arxiv.org/abs/2211.03412).
- [44] Siyu Cheng, Zheng Ren, Hong Li, J. and Hengxin Tan and Ganesh Pokharel and Jonathan M. DeStefano and Elliott Rosenberg and Yucheng Guo and Yichen Zhang and Ziqin Yue and Yongbin Lee and Sergey Gorovikov and Marta Zonno and Makoto Hashimoto, D. and Liqin Ke, Federico Mazzola, Junichiro Kono, R. and Jiun-Haw Chu, Stephen D. Wilson, Ziqiang Wang, and B. and Ming Yi and Ilija Zeljkovic, Nanoscale visualization and spectral fingerprints of the charge order in scv_6sn_6 distinct from other kagome metals, [arXiv:2302.12227](https://arxiv.org/abs/2302.12227).
- [45] M. Tuniz, A. Consiglio, D. Puntel, C. Bigi, S. Enzner, G. Pokharel, P. Orgiani, W. Bronsch, F. Parmigiani, V. Polewczyk, P. D. C. King, J. W. Wells, I. Zeljkovic, P. Carrara, G. Rossi, J. Fujii, I. Vobornik, S. D. Wilson, R. Thomale, T. Wehling, G. Sangiovanni, G. Panaccione, F. Cilento, D. D. Sante, and F. Mazzola, Dynamics and resilience of the charge density wave in a bilayer kagome metal, [arXiv:2302.10699](https://arxiv.org/abs/2302.10699).

- [46] M. H. Christensen, T. Birol, B. M. Andersen, and R. M. Fernandes, Theory of the charge density wave in av_3sb_5 kagome metals, *Phys. Rev. B* **104**, 214513 (2021).
- [47] H. Tan and B. Yan, Abundant lattice instability in kagome metal scv_6sn_6 , [arXiv:2302.07922](https://arxiv.org/abs/2302.07922).
- [48] Y. Hu, X. Wu, Y. Yang, S. Gao, N. C. Plumb, A. P. Schnyder, W. Xie, J. Ma, and M. Shi, Tunable topological dirac surface states and van hove singularities in kagome metal gdv_6sn_6 , *Science Advances* **8**, eadd2024 (2022), <https://www.science.org/doi/pdf/10.1126/sciadv.add2024>.
- [49] Supplementary Materials.
- [50] J. Wong, F. W. Lytle, R. P. Messmer, and D. H. Maylotte, k -edge absorption spectra of selected vanadium compounds, *Phys. Rev. B* **30**, 5596 (1984).
- [51] V. Ilakovac, A. Girard, V. Balédent, P. Foury-Leylekian, B. Winkler, I. Kupčić, H. Berger, A. Bosak, and J.-P. Pouget, Order-disorder type of peierls instability in bav_3s_3 , *Phys. Rev. B* **103**, 014306 (2021).
- [52] D. Reznik, L. Pintschovius, M. Ito, S. Iikubo, M. Sato, H. Goka, M. Fujita, K. Yamada, G. D. Gu, and J. M. Tranquada, Electron-phonon coupling reflecting dynamic charge inhomogeneity in copper oxide superconductors, *Nature* **440**, 1170 (2006).
- [53] H. Haoyu, Y. Jiang, D. Călugăru, X. Feng, and B. A. Bernevig, To be published.
- [54] J. Yu, C. J. Ciccarino, R. Bianco, I. Errea, P. Narang, and B. A. Bernevig, Nontrivial quantum geometry and the strength of electron-phonon coupling, Submitted.
- [55] A. M. Ganose, A. Searle, A. Jain, and S. M. Griffin, Ifermi: A python library for fermi surface generation and analysis, *Journal of Open Source Software* **6**, 3089 (2021).
- [56] G. Kresse and J. Furthmüller, Efficiency of ab-initio total energy calculations for metals and semiconductors using a plane-wave basis set, *Computational materials science* **6**, 15 (1996).
- [57] G. Kresse and J. Hafner, Ab initio molecular dynamics for open-shell transition metals, *Physical Review B* **48**, 13115 (1993).
- [58] G. Kresse and J. Hafner, Ab initio molecular dynamics for liquid metals, *Physical review B* **47**, 558 (1993).
- [59] G. Kresse and J. Hafner, Ab initio molecular-dynamics simulation of the liquid-metal-amorphous-semiconductor transition in germanium, *Physical Review B* **49**, 14251 (1994).
- [60] G. Kresse and J. Furthmüller, Efficient iterative schemes for ab initio total-energy calculations using a plane-wave basis set, *Physical review B* **54**, 11169 (1996).
- [61] J. P. Perdew, K. Burke, and M. Ernzerhof, Generalized gradient approximation made simple, *Physical review letters* **77**, 3865 (1996).
- [62] N. Marzari and D. Vanderbilt, Maximally localized generalized wannier functions for composite energy bands, *Physical review B* **56**, 12847 (1997).
- [63] I. Souza, N. Marzari, and D. Vanderbilt, Maximally localized wannier functions for entangled energy bands, *Physical Review B* **65**, 035109 (2001).
- [64] N. Marzari, A. A. Mostofi, J. R. Yates, I. Souza, and D. Vanderbilt, Maximally localized wannier functions: Theory and applications, *Reviews of Modern Physics* **84**, 1419 (2012).
- [65] G. Pizzi, V. Vitale, R. Arita, S. Blügel, F. Freimuth, G. Géranton, M. Gibertini, D. Gresch, C. Johnson, T. Koretsune, *et al.*, Wannier90 as a community code: new features and applications, *Journal of Physics: Condensed Matter* **32**, 165902 (2020).
- [66] Q. Wu, S. Zhang, H.-F. Song, M. Troyer, and A. A. Soluyanov, Wanniertools: An open-source software package for novel topological materials, *Computer Physics Communications* **224**, 405 (2018).

I. ACKNOWLEDGMENTS

We would like to thank Jiabin Yu and Jonah Herzog-Arbeitman for discussions. D.S. and S.B-C. acknowledge financial support from the MINECO of Spain through the project PID2021-122609NB-C21. H.H. was supported by the European Research Council (ERC) under the European Union’s Horizon 2020 research and innovation program (Grant Agreement No. 101020833). D.Căl. acknowledges the hospitality of the Donostia International Physics Center, at which this work was carried out. D.Căl. and B.A.B. were supported by the European Research Council (ERC) under the European Union’s Horizon 2020 research and innovation program (grant agreement no. 101020833) and by the Simons Investigator Grant No. 404513, the Gordon and Betty Moore Foundation through Grant No.GBMF8685 towards the Princeton theory program, the Gordon and Betty Moore Foundation’s EPiQS Initiative (Grant No. GBMF11070), Office of Naval Research (ONR Grant No. N00014-20-1-2303), Global Collaborative Network Grant at Princeton University, BSF Israel US foundation No. 2018226, NSF-MERSEC (Grant No. MERSEC DMR 2011750). B.A.B. and C.F. are also part of the SuperC collaboration. This research used resources of the Advanced Photon Source, a U.S. Department of Energy (DOE) Office of Science user facility operated for the DOE Office of Science by Argonne National Laboratory under Contract No. DE-AC02-06CH11357.

II. AUTHOR CONTRIBUTION

H.H., Y.J., D.Căl., X.F., and B.A.B. developed the theoretical understanding of experimental observations. H.H., Y.J., and D.Căl. performed analytical analysis of the model. Y.J. and X.F. performed *ab initio* calculations. C.Y., S.R. C.S., and C.F. synthesized the single crystals. A.K. and A.B. carried out the diffuse scattering and IXS measurements at ESRF, and A.H.S. and S.B-C. at APS. S.B-C. analyzed the IXS data. J.S., D.S., and S.B-C. carried out the resonant x-ray scattering and A.B. and D.Ch. the high-resolution x-ray diffraction measurements. A.R., E.V. and S.B-C. performed the ARPES measurements and D.S. analyzed and plotted the data. All authors wrote or provided input to the manuscript. B.A.B and S.B-C. supervised and managed the project.

III. COMPETING INTERESTS

The authors declare no competing interests.